Kalman Filter-Based, Dynamic 3-D Shape Reconstruction for Steerable Needles with Fiber Bragg Gratings in Multi-Core Fibers

Abdulhamit Donder and Ferdinando Rodriguez y Baena

Abstract—Steerable needles are a promising technology to provide safe deployment of tools through complex anatomy in minimally invasive surgery, including tumor-related diagnoses and therapies. For the 3-D localization of these instruments in soft tissue, fiber Bragg gratings (FBGs)-based reconstruction methods have gained in popularity because of the inherent advantages of optical fibers in a clinical setting, such as flexibility, immunity to electromagnetic interference, non-toxicity, the absence of line of sight issues. However, methods proposed thus far focus on shape reconstruction of the steerable needle itself, where accuracy is susceptible to errors in interpolation and curve fitting methods used to estimate the curvature vectors along the needle. In this study, we propose reconstructing the shape of the path created by the steerable needle tip based on the follow-the-leader nature of many of its variants. By assuming that the path made by the tip is equivalent to the shape of the needle, this novel approach paves the way for shape reconstruction through a single set of FBGs at the needle tip, which provides curvature information about every section of the path during navigation. We propose a Kalman Filter-based sensor fusion method to update the curvature information about the sections as they are continually estimated during the insertion process. The proposed method is validated through simulation, *in vitro* and *ex vivo* experiments employing a programmable bevel-tip steerable needle (PBN). The results show clinically acceptable accuracy, with 2.87 mm mean PBN tip position error, and a standard deviation of 1.63 mm for a 120 mm 3-D insertion.

Index Terms—3-D reconstruction, Biomedical, Cancer therapy, Fiber Bragg grating, FBG, Follow-the-leader, Kalman filters, Multi-core fiber, Programmable bevel-tip steerable needle, PBN, Steerable needle, Sensor fusion, Soft tissue, Shape sensing

I. INTRODUCTION

RESEARCH into minimally invasive surgery (MIS) has been growing significantly in the last few decades because of the improved clinical outcomes and reduction in intra- and post-operative risks compared to an equivalent open surgery approach [1]. In the context of MIS, percutaneous intervention is important in tumor-related diagnosis and therapy, where rigid needles are commonly used for various applications, including drug delivery, biopsy, ablation, and brachytherapy. However, when a rigid needle path to a target encounters a critical anatomical feature such as vessels, bones, and nerves, there is no means to avoid it. This eventuality may
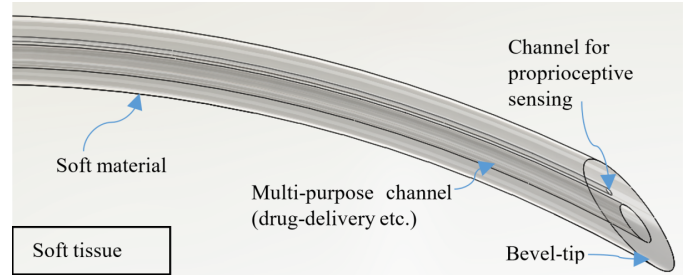
Fig. 1. A bevel-tip steerable needle

cause additional damage and lengthening of the procedure due to the need to extract and reinsert, which is not ideal. Further, there is a possibility of the target tissue moving away from the needle path during the insertion, with a consequent effect on targeting accuracy.

To safely navigate instruments in complex anatomy, a number of steerable needles have been proposed. These types of needle enable steering during navigation into soft tissue to avoid critical anatomical features. Many studies have been conducted to investigate the potential of this promising tool. Different types of steerable needle designs are discussed in [2] and [3], with likely the most widely studied example, the bevel-tip needle, shown in Fig. 1.

The programmable bevel-tip needle (PBN) is a bio-inspired steerable needle based on ovipositing wasps' egg-laying channel structure, through which they can lay their eggs, for example, within wood, by penetrating and steering into it [4]. Similar to this structure, the PBN consists of relatively soft slender segments held together via an "interlocking mechanism", which constrains the relative transverse motion of the segments, as highlighted in Fig. 2. Each segment can be driven independently at the proximal end to achieve relative axial motion, which "programs" the shape of the bevel-tip; thus, the needle can steer through interaction with the surrounding tissue. Illustrations of a 4-segment PBN are shown in Fig. 2. Some of the advantages associated to the PBN design are:

- Tissue deformation is decreased thanks to the reciprocal motion of the PBN segments [5],[6].
- PBNs can be made from more compliant materials compared to the kind of needles requiring transmission of torque from base to tip (as in the case of duty cycle spinning [7]), which leads to a greater steering ability. With more compliant needle materials, follow-the-leader
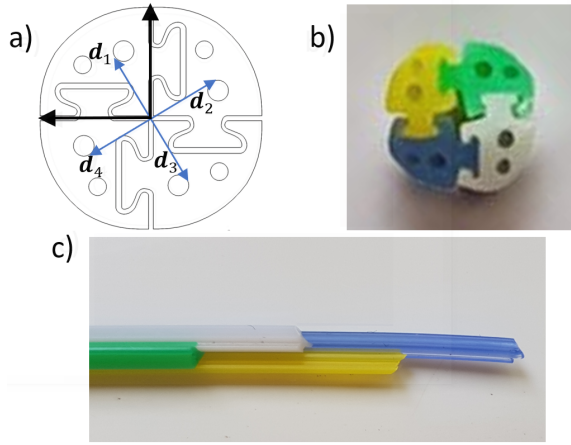
Fig. 2. 4-segment PBN a) Illustration of the cross-section and interlocking segments. The circles represent the working channels that can be used for sensor placement or drug delivery etc. $d_h \in \mathbb{R}^{2 \times 1}$ is the neutral axis discrepancy of the hth segment, $h \in \{1, 2, 3, 4\}$. b-c) 4-segment PBN.

performance is also improved, as it is easier to maintain a suitable difference between needle and substrate stiffnesses to counteract the natural tendency for a needle to straighten once it is bent.

- PBNs can be made magnetic-resonance-imaging (MRI) compatible, as the one used in this study.
- PBNs can steer in full 3-D space without the need for an axial rotation of the needle body [8].

Detailed information about PBNs can be found in [9].

One of the leading open challenges for steerable needles to achieve precise targeting in soft tissue is the need for effective real-time tip tracking. The complications caused by poor needle placement include tissue damage, misdiagnosis, under/overdosing therapy, and unsuccessful treatment [10]. Therefore, needle tracking remains a critical focus area for many researchers in this field [11]. Because of the absence of line-of-sight in percutaneous intervention, proprioceptive tracking methods, such as optical fiber-based shape sensing methods [12], electromagnetic (EM) sensor-based tracking methods [13], and intraoperative medical imaging modalities such as ultrasound [14], [15], fluoroscopy [16], computed tomography (CT) [17], and magnetic-resonance-imaging (MRI) [18], have been studied extensively. Amongst these, the advantages of optical fibers, which are non-ferromagnetic [19], lightweight, small in size, suitable for dynamic-real-time applications, flexible, and radiation-free, make them a promising technology for medical localization.

Shape reconstruction methods based on fiber Bragg grating (FBG)-inscribed optical fibers have been introduced for about a decade [20], [21], [22], [23]. Particularly, improvements arising with the use of multi-core optical fibers (MCFs) [24] have enabled the spread of FBG-based shape reconstruction methods because they eliminate the positioning and alignment difficulties encountered with single-core fibers [25]. FBG-based reconstruction methods in the literature can be grouped into 5 main categories: Frenet-Serret frame-based methods [26], [27], parallel transport frame-based methods [28], [24], piecewise constant curvature methods [22], [29], polynomial

shape-based methods [30], [31], [20] and data-driven regression approaches (DDRA) [32]. Given that the spacing between consecutive FBG sets along an MCF can only be so small, all these methods suffer from the limited number of discrete measurement locations along an MCF.

To address this drawback, interpolation or curve fitting techniques have been suggested to estimate the intermediate curvature vectors in all the methods, but DDRA. These techniques bring along inherent approximation inaccuracies. Similarly, in DDRA, regression performance is a function of the number of measurement locations. Specifically, in all of these methods, as the FBG sets become sparse along the fiber, shape reconstruction accuracy becomes increasingly susceptible to the relative position of bending direction discontinuities with respect to the gratings, as investigated in this study. One way to increase accuracy is to increase the number of FBG sets along the fiber. However, this comes at the expense of higher manufacturing costs, higher calibration complexity, and the increased probability of fiber damage and malfunction [30].

This paper introduces a novel FBG-based shape reconstruction method that ensures that frequent measurements along the fiber length can be acquired even in the presence of only 1 FBG set, which is located at the needle tip, irrespective of the number of bending direction discontinuities along the length of the fiber. Previously proposed approaches focused on reconstructing the steerable needle shape itself, whereas we propose to reconstruct the path created by the steerable needle tip during its insertion into soft tissue instead. This method is based on the follow-the-leader assumption, where the needle body follows the needle tip, which is a valid approximation for most needle embodiments [9], [22], [33]. This approach also enables the reconstruction of the full needle, regardless of where the gratings stop.

In a sense, only using the FBG set at the needle tip is similar to tip tracing methods based on, e.g. an EM sensor embedded within the needle tip. However, while 3-D tip position information can be acquired directly in this way, curvature vectors covering the entire fiber are needed in the case of FBGs to estimate the same information so that the shape is reconstructed from base to tip by numerical integration. We propose a method to acquire the required curvature vectors along the entire needle with only 1 FBG set. Furthermore, we introduce a Kalman Filter (KF)-based algorithm to fuse the information at different discrete time steps, and from different FBG sets in the case where there is more than one along the fiber, which enables the detection of shape changes due to possible soft tissue movements, alongside an increase in reconstruction and tracking accuracy.

Kalman Filtering is one of the most extensively used methods for sensor fusion [34], [35], [36]. The reason for this is that it is well-suited for real-time applications with a stochastic nature. In [34], it was used to combine a flexible catheter's tip position obtained using both ultrasound-based and FBG-based tracking methods. Similarly, to increase needle tip position tracking accuracy, in [37], a KF was used to fuse the information from an optical tracker and an EM sensor. Another study about needle insertion is [38], where the needle tip tracking accuracy was increased by fusing tip position

information from a less accurate but smaller EM sensor at the needle tip and a more accurate but bigger EM sensor at the needle base together with a deflection model. Finally, an extended KF was used for model-based tip pose estimation of a PBN with EM sensors in [39].

The proposed method's performance and other commonly used methods from the literature have been compared in a noise-free simulation environment. Additionally, validation experiments were performed *in vitro* and *ex vivo* with a clinically-sized, medical-grade PBN.

This paper is structured as follows. An introduction of FBG theory is presented in Section II. In Section III, a review of shape reconstruction methods from the literature is given. In Section IV, the proposed shape reconstruction approach is introduced together with the KF-based fusion algorithm. Then, in Section V, the simulation methods are outlined together with their results. This section is followed by Section VI, where the experimental setup and methods are explained, and results are given. In Section VII, the results are discussed, and possible sources of error are presented. Lastly, in Section VIII, conclusions and future work are given.

II. FIBER BRAGG GRATING (FBG) THEORY

FBGs are used as optical strain gauges in a variety of areas such as mechanical, medical, civil, and aerospace engineering applications [40], [41]. An FBG is a grating pattern with a periodic refractive index modulation etched onto an optical fiber, which has the property of reflecting the light of a specific wavelength, the Bragg wavelength, λ_B, which is a function of temperature and strain [42].

$$\lambda_B = 2n_{eff}\Lambda \tag{1}$$

where n_{eff} is the effective refractive index and Λ is the grating period. The relationship between the reflected wavelength shift and change in temperature, ΔT, and strain, ε, is given as follows:

$$\Delta\lambda = \lambda_B((1 - p_e)\varepsilon + (\alpha_\lambda + \alpha_n)\Delta T) \tag{2}$$

where p_e is the photo-elastic coefficient, and α_λ and α_n are the thermal expansion coefficient and the thermo-optic coefficient, respectively [42].

When the temperature change can be assumed to be 0, the axial strain on an FBG can be computed as:

$$\varepsilon = \frac{\Delta\lambda}{\lambda_B(1 - p_e)} \tag{3}$$

Assuming that the fiber is in pure bending and behaves as a uniform, symmetric, linear Kirchhoff rod [43], the axial strains due to bending at each core can be derived from mechanics principles as follows [44]:

$$\varepsilon_j(s) = -\kappa(s)\delta_j(s) \tag{4}$$

where s represents the arc length parameter along the fiber $(0, L)$, where L is the length of the fiber, $\varepsilon_j(s)$ is the strain at the jth core, with $j \in 1, ..., G$, and G is the total number of off-centered cores. $\kappa(s)$ is the curvature, and $\delta_j(s)$ is the
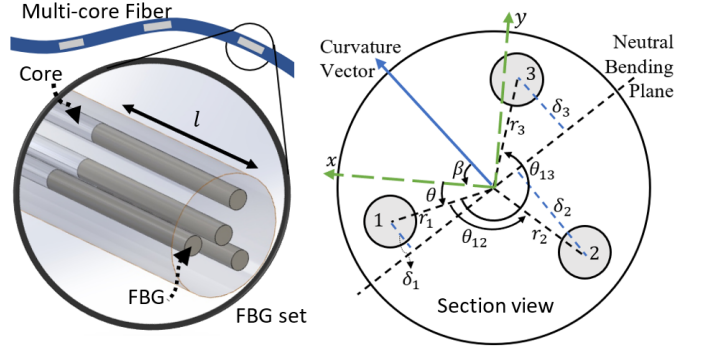

Fig. 3. Left: FBG-inscribed MCF including 4 cores: 1 centered, 3 off-centered. Right: MCF with 3 off-centered cores in section view (an FBG set). The cores are denoted by the numbers: 1, 2, 3. r_j is the radial distance from the MCF center to the center of the jth core, where $j \in \{1, 2, 3\}$. δ_j is the distance between the neutral bending plane and the jth core center. The local frame is denoted by the x, y axes. θ is the angular offset from the local x axis to the 1st core. β is the angular offset from the curvature vector to the local x axis. θ_{12} is the angle from the 1st core to the 2nd core. Similarly, θ_{13} is the angle from the 1st core to the 3rd core.

distance between the center of the jth core and the neutral bending plane, as shown in Fig. 3. Therefore, (4) can be written as follows:

$$\varepsilon_j(s) = -\kappa(s)r_j cos(\beta(s) + \theta + \theta_{1j}) + \varepsilon_0(s) \tag{5}$$

where r_j is the radial distance between the fiber center and the center of the jth core, $\beta(s)$ is the angular offset from the curvature vector to the x axis of the local frame, and θ is the angular offset from the x axis of the local frame to the 1st core. Similarly, θ_{1j} is the angular offset from the 1st core to the jth core, with $\theta_{11}(s) = 0$. The curvature vector is defined with $\kappa(s)$ being the magnitude and $\beta(s)$ the bending direction of the curvature vector. It can also be defined as the rate of change of the curve's unit tangent vector with respect to s: $d\boldsymbol{T}(s)/ds$. The strain bias $\varepsilon_0(s)$ is due to additional axial strain and temperature change. When a temperature change can be assumed to affect all the gratings in an FBG set equally due to the proximity of the fibers (as in the case of MCFs), the effect of it can be assumed to be compensated by the strain bias [45], [46]. Additionally, in the case of separation between the neutral axes of a needle and the fiber, it is instrumented with, the additional axial strain reflects on $\varepsilon_0(s)$ as well. (5) is a general formula, which is valid for any number of cores along a fiber in any configuration, symmetrical or asymmetrical. An example configuration is shown in Fig. 3, with 3 cores to illustrate the parameters used in (5).

The locations of the FBG sets along a fiber are known *a priori*. To compute the curvature vector, at least 3 linearly independent (i.e., not symmetric about the fiber center), off-centered cores are necessary. As many equations as the number of such cores can be obtained from (5), which can be solved simultaneously to compute the curvature value, $\kappa(s)$, bending direction, $\beta(s)$, and $\varepsilon_0(s)$. Note that at least 3 equations are required for this calculation ($G \in \mathbb{Z}_{\geq 3}$). In the presence of more than 3 available cores, the equations from all of the cores can be used to increase accuracy and improve robustness via

redundancy. In matrix form, (5) can be written for G cores as follows:

$$\underbrace{\begin{bmatrix} \varepsilon_1(s) \\ \vdots \\ \varepsilon_G(s) \end{bmatrix}}_{\boldsymbol{\varepsilon}(s)} = \underbrace{\begin{bmatrix} -r_1 cos(\theta_{11} + \theta) & r_1 sin(\theta_{11} + \theta) & 1 \\ \vdots & \vdots & \vdots \\ -r_G cos(\theta_{1G} + \theta) & r_G sin(\theta_{1G} + \theta) & 1 \end{bmatrix}}_{\boldsymbol{M}} \underbrace{\begin{bmatrix} \kappa(s)cos\beta(s) \\ \kappa(s)sin\beta(s) \\ \varepsilon_0(s) \end{bmatrix}}_{\boldsymbol{\alpha}(s)}$$

(6)

Solving for $\boldsymbol{\alpha}(s)$:

$$\boldsymbol{\alpha}(s) = \boldsymbol{M}^\dagger \boldsymbol{\varepsilon(s)} \qquad (7)$$

where $\boldsymbol{M}^\dagger$ is Moore-Penrose pseudo-inverse of $\boldsymbol{M}$ (Note that $\boldsymbol{M}$ is not necessarily a square matrix).

As a result:

$$\kappa(s) = \sqrt{\boldsymbol{\alpha}_1(s)^2 + \boldsymbol{\alpha}_2(s)^2} \qquad (8)$$

$$\beta(s) = atan_2(\boldsymbol{\alpha}_2(s), \boldsymbol{\alpha}_1(s)) \qquad (9)$$

The torsion can be approximated with numerical derivation:

$$\tau(s) = \frac{\beta(s) - \beta(s - \Delta s)}{\Delta s} \qquad (10)$$

$\kappa(s)$, $\beta(s)$, and $\tau(s)$ are used for shape reconstruction, as reviewed in the following section.

III. FBG-BASED SHAPE RECONSTRUCTION AND TIP TRACKING METHODS

Shape reconstruction methods require the information from the strain values or the curvature vectors along the entire fiber. However, only sparse measurements can be obtained with discrete FBG sets, and, therefore, an interpolation/curve fitting method is required to estimate the intermediate values. Although, in this study, we propose a shape reconstruction method that does not require the estimation of the intermediate strain values or curvature vectors in between the FBG sets, an overview of interpolation and curve fitting methods is given in Section III-A for completeness. A review of shape reconstruction methods is presented in Section III-B.

A. Interpolation / Curve Fitting Methods

In this section, interpolation and curve fitting methods based on discrete FBG measurements are reviewed from the literature to help interpret the comparative study in Section V.

The accuracy of fiber tip pose estimation highly depends on selecting the most suitable interpolation/curve fitting methods to determine the intermediate strain values or curvature vectors between the discrete FBG sets. For example, a small curvature error due to the applied interpolation method will result in a large position error at the tip due to error accumulation during numerical integration. Henken *et al.* [46] presented an error analysis of standard interpolation methods. They used the curvature vector as the interpolation parameter, as in most of the studies in the literature. However, Jäckle *et al.* [45] proposed interpolating the strain because of its continuity along the fiber, when considering the possible discontinuity in the bending direction.

A simulation study comparing the proposed method with the methods requiring interpolation is given in Section V, alongside an analysis investigating the effect of discontinuities in the bending direction to shape sensing accuracy.

B. FBG-Based Shape Reconstruction and Fiber Tip Position Estimation Methods

In this section, shape reconstruction methods from the literature, based on discrete FBG measurements, are reviewed. These methods show promise, but their accuracy is susceptible to errors of the interpolation methods.

1) Frenet-Serret frame-based methods: This shape reconstruction method is based on the Frenet-Serret equations [47]:

$$\frac{d\boldsymbol{\gamma}(s)}{ds} = \boldsymbol{T}(s), \quad \frac{d\boldsymbol{N}(s)}{ds} = -\kappa(s)\boldsymbol{N}(s) + \tau(s)\boldsymbol{B}(s)$$

$$\frac{d\boldsymbol{T}(s)}{ds} = \kappa(s)\boldsymbol{N}(s), \quad \frac{d\boldsymbol{B}(s)}{ds} = -\tau(s)\boldsymbol{N}(s) \qquad (11)$$

where $\boldsymbol{\gamma}(s)$ is the position vector in $\mathbb{R}^3$, $\boldsymbol{T}(s)$ the unit tangent vector, $\boldsymbol{N}(s)$ the unit normal vector, $\boldsymbol{B}(s)$ the unit binormal vector, $\kappa(s)$ the curvature value, and $\tau(s)$ the torsion of the curve (i.e., the rate of change of bending direction, $\beta(s)$).

This method requires that the curve to be reconstructed must be with non-zero curvature along its length; otherwise, it generates ambiguity in the definition of $\boldsymbol{N}(s)$ and $\boldsymbol{B}(s)$, because $\tau(s)$ is not defined in the case of zero curvature [48]. After estimating intermediate curvature values in between the FBG sets using one of the methods in Section III-A, the shape is constructed by the integration of vectors $\boldsymbol{T}(s)$.

2) Parallel transport frame-based methods: This shape reconstruction method is based on the parallel transport frame [49], which satisfies the following frame equations:

$$\frac{d\boldsymbol{\gamma}(s)}{ds} = \boldsymbol{T}(s), \quad \frac{d\boldsymbol{T}(s)}{ds} = \kappa_1(s)\boldsymbol{N}_1(s) + \kappa_2(s)\boldsymbol{N}_2(s)$$

$$\frac{d\boldsymbol{N}_1(s)}{ds} = -\kappa_1(s)\boldsymbol{T}(s), \quad \frac{d\boldsymbol{N}_2(s)}{ds} = -\kappa_2(s)\boldsymbol{T}(s) \quad (12)$$

where $\boldsymbol{T}(s)$ is the unit tangent vector and $\boldsymbol{N}_1(s)$, $\boldsymbol{N}_2(s)$ the unit normal vectors. $\kappa_1(s)$ and $\kappa_2(s)$ describe the change of $\boldsymbol{T}(s)$ in the $\boldsymbol{N}_1(s)$ and $\boldsymbol{N}_2(s)$ directions at arc length position s and are calculated as follows:

$$\kappa_1(s) = \kappa(s)cos(\beta(s))$$

$$\kappa_2(s) = \kappa(s)sin(\beta(s)) \qquad (13)$$

This method is advantageous over the Frenet-Serret frame since it is defined for every curve, including zero curvature curves. $\boldsymbol{N}_1(s)$, and $\boldsymbol{N}_2(s)$ change slightly along the curve upon being chosen arbitrarily at the needle base, such that the frame components are perpendicular to one another. The shape is reconstructed in a similar way as in the case of Frenet-Serret frame-based reconstruction.

3) Piecewise constant curvature method: Roesthuis *et al.* [22] proposed a reconstruction method based on piecewise constant curvature elements. The $(i+1)^{th}$ element expressed in previous element's frame is created with a constant curvature vector:

$$\boldsymbol{p}_{i+1}^i = \begin{bmatrix} dx & dy & dz \end{bmatrix}$$

$$= \begin{bmatrix} \rho_i sin(d\theta_i) & 0 & \rho_i cos(d\theta_i) - \rho_i \end{bmatrix} \quad (14)$$

where dx, dy, and dz are the cartesian distances, ρ_i is the radius of curvature, and $d\theta_i = ds/\rho_i$ with ds being the length of the curvature element. Therefore, the whole shape is obtained by directly integrating these discrete elements. Linear spline interpolation was used to estimate the intermediate curvature values in their study.

4) Polynomial shape-based methods: Seifabadi *et al.* [30] proposed fitting an nth order polynomial to n curvature values obtained from FBG measurements. The displacement along the fiber is obtained by integrating the polynomial twice and applying the boundary conditions; $y'(0) = 0$ and $y(0) = 0$.

$$y''(s) = \kappa(s) \quad (15)$$

where $y(s)$ is the deflection, $y'(s)$ and $y''(s)$ are the first and second derivatives of deflection, and $\kappa(s)$ is the curvature value at arc length s. In this method, the intermediate curvature values are accessed via the fitted continuous polynomial.

5) Data-driven tip position estimation approaches: Sefati *et al.* [32] proposed a regression-model-based method which is sensor-model-independent and only requires the raw data of the FBG wavelengths to estimate the tip position of a continuum dexterous manipulator. Although this method does not require the estimation of intermediate strain values or curvature vectors, the tip position estimation performance is expected to increase as the number of measurements increases along the fiber.

IV. MATERIALS AND METHODS

Regardless of the total number of FBG sets that an MCF inside a needle possesses, we propose that only the FBG set at the fiber's tip is used to reconstruct the shape during soft tissue navigation. In the case of more than 1 available FBG set, the information from different sets can then be fused using the method proposed in Section IV-C.

Because of the "follow-the-leader" nature of steerable needles, we assume that the needle's shape overlaps with the path created by its tip during navigation into soft tissue. Therefore, instead of reconstructing the fiber shape, the shape of the path covered by the fiber's tip is reconstructed. The curve created during navigation of the MCF tip is modeled as a regular unit-speed space curve in $\mathbb{R}^3$ with $i \in \{1, ..., N_k\}$ denoting the discrete curve points. N_k is the total number of curve points at discrete sampling time k: t_k. The fiber is assumed to be in pure bending, and it is modeled as a uniform-density, symmetric (circular cross-section), linear Kirchhoff rod [43].

A. Obtaining Curvature Pairs

The curve points are assumed to be fixed with respect to the soft tissue (and not with respect to the needle). Therefore, as the needle advances into the soft tissue, the curvature vectors at newly covered ground are calculated at each time step (Fig. 4). Let $n_k \in \mathbb{Z}_{\geq 0}$ be the number of curve points created (i.e., positions of which are calculated) at t_k in the case of the advancement of the needle into soft tissue. Let $\tilde{\boldsymbol{c}}_k = \begin{bmatrix} \tilde{\kappa}_{1,k} & \tilde{\kappa}_{2,k} \end{bmatrix}^T \in \mathbb{R}^{2 \times 1}$ be the curvature pair as given in (13) calculated after obtaining the segment's curvature vectors using wavelength readings at t_k.

Also, let $\hat{\boldsymbol{c}}_k^i = \begin{bmatrix} \kappa_{1,k}^i & \kappa_{2,k}^i \end{bmatrix}^T \in \mathbb{R}^{2 \times 1}$ be the curvature pair of the ith curve point at t_k. The curvature pairs corresponding to newly covered ground, and N_k are obtained as follows.

$$\hat{\boldsymbol{c}}_k^i = \tilde{\boldsymbol{c}}_k \quad (16)$$

$$N_k = N_{k-1} + n_k \quad (17)$$

B. Compensation for the Lead-Out Length

We call the length between the tip FBG set and the needle tip the "lead-out" length, as shown in Fig. 4 as l_{lead}. This length is required for three reasons: (i) to accommodate the needle tip's beveled shape, (ii) to protect the end of the fiber, (iii) to position the tip FBG set at a point where the relevant curvature of the needle tip can be measured. The curvature of the needle tip is best measured at a small distance from its very tip due to the soft needle material, and the tolerances between the outer diameter of the fiber and the diameter of the needle's working channel. This situation is illustrated in Fig. 5. Therefore, $\tilde{\boldsymbol{c}}_k$ is also assigned to curvatures corresponding to this length.
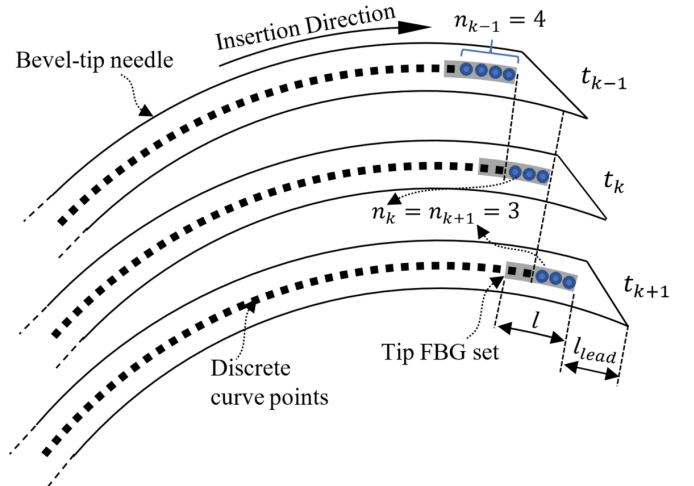

Fig. 4. 2-D Illustration of needle insertion into soft tissue. A bevel-tip needle is illustrated at three successive time steps. The FBG set with the length of l is shown at the tip in grey. The discrete curve points are assumed to be fixed with respect to the soft tissue (not with respect to the needle). The curve points created at the current time step are shown in blue circles, whereas the curve points created at the previous time steps are shown in black squares. The distance between the needle tip and the FBG set is called lead-out length, l_{lead}, and the curvature values of which can be estimated by extrapolation. $n_k \in \mathbb{Z}_{\geq 0}$ is the number of curve points created at t_k.
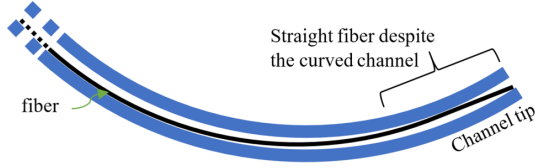
Fig. 5. A needle working channel. The last bits of fibers tend to be straight even if the needle curves because of the soft needle material and the clearance between the fiber and the channel. The width of the channel is exaggerated for clarity.

C. Kalman Filter-Based Sensor Fusion

In this study, we use a KF to obtain more reliable estimates of the curvatures along the fiber length. The measurements at a time step are used to create or update the curve points of the ground that is covered by the FBG set/sets at that time step. Let M be the total number of FBG sets along a fiber, and FBG_m, $m \in \{1, ..., M\}$, be the mth FBG set from the fiber tip (e.g., FBG_1 is the FBG set at the fiber tip) as shown in Fig. 6. As a needle is inserted into a soft tissue, the very first shape reconstruction is obtained by FBG_1 as described in the previous sections. If there are other FBG sets, once FBG_2 reaches a curve point of the reconstructed path, the curvature information from FBG_1 is fused with that of FBG_2 by means of a KF. This is repeated as FBG_2 continues to take measurements or other FBG sets start taking measurements from that curve point. This procedure is performed for all the curve points along the fiber. The information from an FBG set is used to update the curvature information of the curve points covered by any part of its length. This process enables shape reconstruction at a length which is greater than the length of the sensorized segment of the fiber.

The KF-based sensor fusion consists of two steps: prediction and correction, which require the formulation of a process model with process noise, and a measurement model with measurement noise, respectively [50].

The first state vector, i.e., curvature pair values, of any curve point is always obtained with FBG_1 because the path is created by the tip. After that, the state vector is updated by means of the KF if this curve point is covered by one of the FBG sets. Otherwise, the same values are used for the next time step's state vector.

The process model is defined as a linear stochastic equation:

$$\hat{\boldsymbol{c}}_k^i = \hat{\boldsymbol{c}}_{k-1}^i + \boldsymbol{w} \tag{18}$$
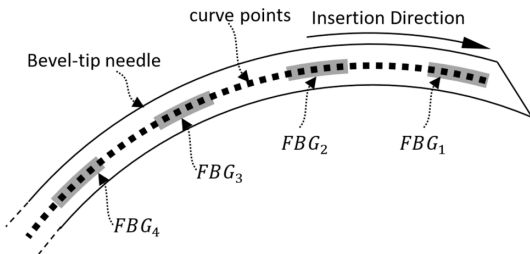

Fig. 6. 2-D Illustration of a bevel-tip needle with an MCF possessing more than one FBG set along its length. The discrete curve points are assumed to be fixed to the soft tissue.

where $\boldsymbol{w} \sim \boldsymbol{N}(0, \boldsymbol{Q}) \in \mathbb{R}^{2 \times 1}$ is the process noise vector represented by zero-mean Gaussian distribution with $\boldsymbol{Q} \in \mathbb{R}^{2 \times 2}$ being the covariance matrix. The reason for process noise uncertainties arises from the possible non-zero error in the follow-the-leader assumption.

The measurement model is defined as follows:

$$\boldsymbol{z}_k^i = \hat{\boldsymbol{c}}_k^i + \boldsymbol{v} \tag{19}$$

where $\boldsymbol{z}_k^i$ is the measurement variable and $\boldsymbol{v} \sim \boldsymbol{N}(0, \boldsymbol{R}) \in \mathbb{R}^{2 \times 1}$ is the measurement noise vector represented by a zero-mean Gaussian distribution with $\boldsymbol{R} \in \mathbb{R}^{2 \times 2}$ being the covariance matrix.

The covariance matrices $\boldsymbol{Q}$ and $\boldsymbol{R}$ are determined as per description at the end of this subsection. Based on the process and the measurement models, the filter's prediction and correction steps are applied at each sampling loop to correct the state estimates.

Prediction step: In this step, the *a priori* system state at t_k is estimated:

$$\hat{\boldsymbol{c}}_k^{-,i} = \hat{\boldsymbol{c}}_{k-1}^i \tag{20}$$

Given the initial estimate, the *a priori* error covariance $\boldsymbol{P}^{-,i} \in \mathbb{R}^{2 \times 2}$, which is the combination of process noise and the propagation of the error covariance, $\boldsymbol{P}_{k-1}^i$, from the previous state, is estimated as follows:

$$\boldsymbol{P}_k^{-,i} = \boldsymbol{P}_{k-1}^i \boldsymbol{Q} \tag{21}$$

Correction Step: In this step, *a priori* estimates of the system state and error covariance are updated with the Kalman Gain, $\boldsymbol{K}_k^i \in \mathbb{R}^{2 \times 2}$.

$$\boldsymbol{K}_k^i = \boldsymbol{P}_k^{-,i}(\boldsymbol{P}_k^{-,i} + \boldsymbol{R})^{-1}$$
$$\hat{\boldsymbol{c}}_k^i = \hat{\boldsymbol{c}}_k^{-,i} + \boldsymbol{K}_k^i(\boldsymbol{z}_k^i - \hat{\boldsymbol{c}}_k^{-,i}) \tag{22}$$
$$\boldsymbol{P}_k^i = (\boldsymbol{I}_2 - \boldsymbol{K}_k^i)\boldsymbol{P}_k^{-,i}$$

where $\boldsymbol{I}_2 \in \mathbb{R}^{2 \times 2}$ is an identity matrix. If a curve point is not covered by any FBG set at t_k, $\hat{\boldsymbol{c}}_{k-1}^i$ and $\boldsymbol{P}_{k-1}^i$ are directly assigned to $\hat{\boldsymbol{c}}_k^i$ and $\boldsymbol{P}_k^i$ respectively:

$$\hat{\boldsymbol{c}}_k^i = \hat{\boldsymbol{c}}_{k-1}^i \tag{23}$$

$$\boldsymbol{P}_k^i = \boldsymbol{P}_{k-1}^i \tag{24}$$

Calculation of the Covariance Matrices: In order to determine the matrix $\boldsymbol{R}$, which is defined to be the same for all the FBG sets, the needle is driven along a constant curvature trajectory, and $\boldsymbol{R}$ is calculated using the curvature pair error values, $\boldsymbol{e}_a \in \mathbb{R}^{A \times 2}$, which are given as follows:

$$\boldsymbol{e}_a = \tilde{\boldsymbol{c}}_a - \frac{1}{A}\sum_{f=1}^{A}\tilde{\boldsymbol{c}}_f \tag{25}$$

where $a \in \{1, ..., A\}$, A being the total number of measurements for all of the FBG sets, and $\tilde{\boldsymbol{c}}_a \in \mathbb{R}^{1 \times 2}$ the ath curvature pair measurement.

$\boldsymbol{Q}$ is defined as follows:

$$Q = \xi \begin{bmatrix} \sigma_{\kappa_1}^2 & \sigma_{\kappa_1 \kappa_2} \\ \sigma_{\kappa_1 \kappa_2} & \sigma_{\kappa_2}^2 \end{bmatrix} \tag{26}$$

where $\sigma_{\kappa_1}^2$ and $\sigma_{\kappa_2}^2$ are the process error variances of the curvatures, which are assumed to be equal to each other, given that the PBN has a symmetric cross-section. ξ is a variable scaling parameter defined to scale the matrix at the first prediction step when a new FBG reaches the position, and it is used to give more weight to the newer measure:

$$\xi = \begin{cases} \rho, & \text{First prediction step of a new FBG} \\ 1, & \text{otherwise} \end{cases} \tag{27}$$

In order to collect data to be used to determine the unknowns of the matrix Q, a steerable needle instrumented with an optical fiber is inserted into a soft tissue phantom, and curvature values are collected from FBG sets throughout the insertion. The three unknowns, ρ, $\sigma_{\kappa_1}^2$ and $\sigma_{\kappa_1 \kappa_2}$, the last of which is the co-variance of the curvature process error, are optimized with the interior point algorithm [51] so the mean tip position error between the ground truth and the reconstruction is minimized.

Although the curvature pairs are used as the state variables, curvature vectors, FBG strain values, or the ratios between wavelength shifts and Bragg wavelengths would also be suitable. This is because these are independent variables describing the state of curve points, and the shape can be reconstructed using the curvatures calculated using them, as explained in Section II and Section III. However, strain and wavelength values are less intuitive for the intended use-case compared to others, and using curvature vectors would require tuning three elements of matrix Q instead of two elements, as in this study, since the elements on the main diagonal (the curvature and the bending direction) cannot be assumed to be equal.

A single evaluation of shape reconstruction performance for an MCF with KF, sampled every 50 μm (20 Hz at 1 mm·s⁻¹) throughout the navigation process, running on an Intel(R) Core(TM) i7-10510U CPU @ 1.80 GHz - 2.30 GHz with MATLAB 2020b, takes an average of 23 ms in the presence of only the tip FBG set (before the other FBG sets reach the points created by the tip FBG set) and 88 ms in the presence of eight FBG sets, each of which is assumed to be 5 mm long.

D. Application to Needle Steering

If a steerable needle navigates in soft tissue in a follow-the-leader fashion and can be instrumented with an FBG-inscribed multi-core optical fiber, the proposed methods can be used for shape reconstruction. In this study, the validation experiments were performed using a PBN.

The zero-torsion and follow-the-leader assumptions, we make in this study for PBNs, are considered acceptable according to the PBN-tissue interaction model developed and validated in [9].

When a PBN where all the segments contain an MCF is inserted into a soft tissue, each segment's shape can be reconstructed individually with the proposed method. Also,

the shape of the PBN at t_k can be assumed to be always equivalent to that of the segment that is further ahead (i.e., the leading segment). However, we propose integrating the curvature information from all the segments to increase accuracy by averaging the curvatures corresponding to each curve point of the PBN. Let $p \in \{1, ..., N_k^{PBN}\}$ correspond to discrete curve points along the PBN, where N_k^{PBN} is the total number of the curve points. Also, let the superscript $v \in \{1, ..., g_k^p\}$ denote the vth curve, created by one of the segment tips, of which one curve point corresponds to p, with g_k^p being the total number of the curves. This parametrization allows the reconstruction to complete successfully if the segments tips are not aligned, a configuration that is essential to create curvature.

Therefore, the corresponding curvatures for all PBN curve positions are averaged to calculate the resultant curvatures along the PBN.

Considering a PBN's curvilinear navigation, a path-dependent discrepancy is expected between the segments' navigation lengths because of the separation between their neutral axes. A similar discrepancy is also expected between the curves created by the segment tips. Therefore, this discrepancy must be taken into account when matching the corresponding curvatures along the PBN. This issue was discussed by Watts *et al.* in [9], where they proposed an open-loop compensation method for the case where the curve points of the PBN centerline are known, which is the inverse of what is available in this study, where the curve points of the individual segments are known. Therefore, their algorithm was adapted with additional steps in our study to compensate for this discrepancy and, thus, match the steps of individual curves corresponding to curve points along the PBN. The updated algorithm is given in Algorithm 1.

Let $d_h \in \mathbb{R}^{2 \times 1}$ be the neutral axis discrepancy of the hth segment, $h \in \{1, 2, 3, 4\}$, as shown in Fig. 2 and $\hat{c}_k^{i,h} \in \mathbb{R}^{2 \times 1}$ be the curvature value pair of the hth segment's i^{th} curve point. Therefore, the curves' curvature pairs corresponding to PBN curve points are calculated with Algorithm 1, and the curvature pairs, $\bar{c}_k^{PBN,p} \in \mathbb{R}^{2 \times 1}$, of the PBN are calculated by averaging the curvature pairs corresponding to PBN curve points:

$$\bar{c}_k^{PBN,p} = \frac{1}{g_k^p} \sum_{v=1}^{g_k^p} c_k^{v,p} \tag{28}$$

Finally, the PBN shape is reconstructed with the resultant curvature pairs, $\bar{c}_k^{PBN,p}$, based on the parallel transport frames-based method given in Section III-B because of its stability and noise handling capabilities, making it advantageous over the other methods, as suggested in [45].

E. Calibration and Curvature Value Correction

Firstly, calibration is required to determine the FBG wavelengths at zero-strain, which are to be used as Bragg wavelengths in (3). These are determined by placing the fiber into a linear guide. Secondly, calibration is needed to determine the angular position of the 1st core with respect to the local frame as denoted by θ in Fig. 3. This is determined by placing the fiber into a 2-D curved guide with a known bending direction.

Algorithm 1 An algorithm to calculate PBN curvature pairs by matching the curve points of individual curves. All the parameters are for the discrete time step, t_k

---

Input: Neutral axis separations: $\boldsymbol{d}_h$, $h \in \{1,2,3,4\}$, Curvature value pairs: $\hat{\boldsymbol{c}}_k^{i,h}$, The total number of curve points of the curves created by the segment tips: N_k^h

Output: g_k^p, and all the curves' curvature pairs corresponding to PBN curve points: $\boldsymbol{c}_k^{v,p}$

1: $l_h = N_k^h + \sum_{i=1}^{N_k^h} (\boldsymbol{d}_h \cdot \hat{\boldsymbol{c}}_k^{i,h})$ $\quad \triangleright$ Corresponding length of curve h at PBN centerline
2: $L = \text{Index of Max}(l_1, l_2, l_3, l_4)$ $\quad \triangleright$ Leading segment
3: $T_h = 0$
4: **for all** p **do** $\quad \triangleright N_k^{PBN} = N_k^L$
5: $\quad g_k^p = 0, \quad v = 0$
6: $\quad$ **for** $h = 1,2,3,4$ **do**
7: $\quad\quad T_h = T_h + (1 - \boldsymbol{d}_h \cdot \frac{\hat{\boldsymbol{c}}_k^{p,L}}{\|1 + \hat{\boldsymbol{c}}_k^{p,L} \cdot \boldsymbol{d}_L\|})(1 + \boldsymbol{d}_L \cdot \hat{\boldsymbol{c}}_k^{p,L})$
8: $\quad\quad$ **if** $N_k^h \geq T_h$ **then**
9: $\quad\quad\quad g_k^p = g_k^p + 1, \quad v = v + 1$
10: $\quad\quad\quad \boldsymbol{c}_k^{v,p} = \hat{\boldsymbol{c}}_k^{round(T_h),h}$
11: $\quad\quad$ **end if**
12: $\quad$ **end for**
13: **end for**

Additionally, as proposed in [45], since the photo-elastic coefficient, p_e, could be biased, a correction parameter, $c_{correct}$, is determined to calculate the curvature values more accurately, as follows:

$$\kappa_{real} = c_{correct}\kappa_{measured} \tag{29}$$

The parameter, $c_{correct}$, is determined for each of the FBG sets separately by placing the fiber in 2-D curved guides with known curvatures (κ_{real}) and comparing it with the ones obtained from FBG measurements ($\kappa_{measured}$). Therefore, $c_{correct}$ and the angle θ (the angular offset from the x axis of the local frame to the 1$^\text{st}$ core - Fig. 3) can be determined simultaneously. This calibration procedure needs to be performed for each fiber only once after fiber-needle fixation.

V. SIMULATIONS

According to Henken *et al.* [46], shape errors are lowest with cubic spline interpolation, which was used in this simulation study. The shape was reconstructed with the interpolation of the strain values corresponding to virtual FBG set locations. Several simulations were performed to show the advantages of the proposed method over the methods requiring interpolation in a noise-free environment. A steerable needle is assumed to be driven into three different shapes consisting of two parts with zero torsion along their length. The radius of curvature of the first parts is 90 mm. The radius of curvature of the second parts, which are in planes perpendicular to the first segments, is 120 mm.

Shape 1: both two parts are 49 mm long,
Shape 2: the first part is 44 mm long, and the second part is 54 mm long,

Shape 3: the first part is 54 mm long, and the second part is 44 mm long.

At each time instant during the insertions, the ground truth curvatures and strain values corresponding to the virtual FBG sets' locations are considered to be the measurements obtained from them.

A. Shape Reconstruction with Interpolation

Eight virtual pointwise FBG sets were modeled with 14 mm center-to-center distances. The simulation flow chart is given in Fig. 7. The curvatures and the strain values corresponding only to the 8 virtual FBG set locations on the ground truth curve were used. These FBG sets are illustrated in Fig. 8 along with the 3 shapes. These pointwise values were interpolated, and the parallel transport frame method was used for shape reconstruction since it is advantageous over the other methods, as described in Section IV-D. Lastly, the tip positions of the reconstructed curves were compared with that of the ground truths.

B. Shape Reconstruction with The Proposed Method

A simulation using the proposed method was conducted with only one pointwise FBG set at the fiber tip with an insertion speed of 1 mm·s⁻¹ and a sampling frequency of 100 Hz, which results in sampling at each 10 μm of the insertion trajectory. No interpolation or curve fitting was used. Also, since the simulation was conducted in a noise-free environment, the KF was not used.

C. Results

The results of the simulations are given in Table I. The small error of the reconstruction without interpolation is clearly due to the high sampling frequency throughout the insertion trajectory.
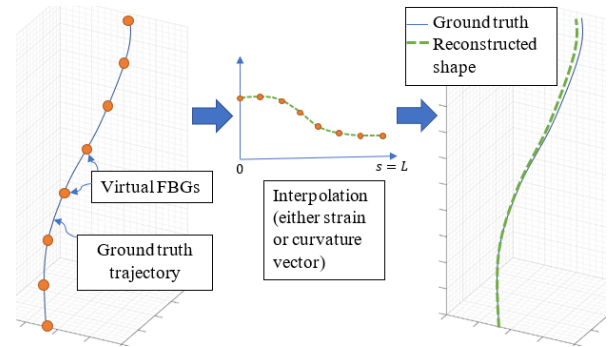

Fig. 7. Shape Reconstruction with a Method Requiring Interpolation.

TABLE I
SIMULATION STUDY TIP POSITION ERRORS [MM] WHEN A STEERABLE NEEDLE IS DRIVEN INTO THREE SHAPES.

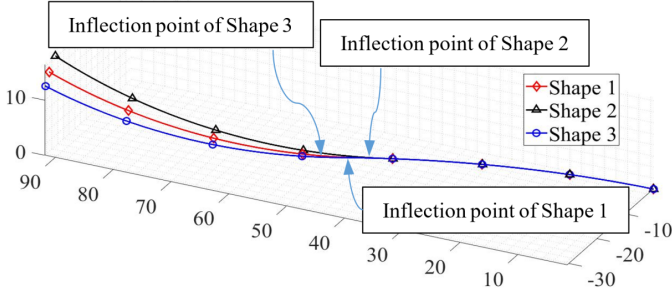|	Shape 1	Shape 2	Shape 3
Shape recon. with interpolation	0.6	3.26	1.65
Shape recon. with proposed method	0.048	0.094	0.040

Fig. 8. Illustration of the three shapes with the virtual FBG sets used in the simulation study. Markers represent the locations of the pointwise FBGs. Dimensions are in millimeters.

VI. EXPERIMENTAL METHODS

In vitro and *ex vivo* tests were conducted to validate the proposed shape reconstruction methods. Two error measures were defined to quantify performance, as follows:

1) The absolute difference between the tip of the reconstruction and the corresponding ground truth point:

$$e_{pos}^{tip} = \left\| \gamma_{recon}^{tip} - \gamma_{gt}^{tip} \right\| \tag{30}$$

where the "gt" subscript is for "ground truth", and γ_{gt}^{tip} is the ground truth point corresponding to the reconstructed tip point γ_{recon}^{tip}

2) The absolute angular difference between the orientations at the tips of the ground truth and the reconstructed curve:

$$e_o^{tip} = cos^{-1} \left(\frac{r_{gt}^{tip} \cdot r_{recon}^{tip}}{\left\| r_{gt}^{tip} \right\| \left\| r_{recon}^{tip} \right\|} \right) \tag{31}$$

where r_{recon}^{tip} is the reconstructed tip orientation vector, and r_{gt}^{tip} is the ground truth orientation vector corresponding to the reconstructed tip orientation. Minimizing this error is essential when the intervention, such as drug delivery or tissue ablation, must be performed at a given tip orientation [52].

The tip errors are expected to be the greatest because of the error accumulation in numerical integration.

A. Setup

The experiments were conducted utilizing a clinically-sized, medical-grade, 4-segment PBN (Fig. 2), with all the segments instrumented with FBG-inscribed MCFs (FBGS International NV, Geel, Belgium). The specifications of the MCFs are given in Table II, and an MCF cross-section is illustrated in Fig. 9. The FBGs inscribed with the Draw Tower Gratings (DTG®) method were chosen because fibers of relatively high strength are required in the dynamic experiments [53]. The FBG data acquisition was performed with a sampling frequency of 50 Hz. In addition to the KF, a moving average filter using the data of 5 time steps was utilized to further mitigate the effect of noise.

Electromagnetic sensors (NDI - Aurora System - Ontario, Canada) with 5 degrees of freedom, including pitch, yaw, and

TABLE II
MCF SPECIFICATIONS - FBGS INTERNATIONAL NV (GEEL, BELGIUM)

Production technique	Draw Tower Gratings (DTG®)
Operating temperature	-20°C to 200°C
Wavelength configurations of the 4 MCFs	MCF 1: 1513.0nm - 1529.8nm
	MCF 2: 1532.2nm - 1549.0nm
	MCF 3: 1551.4nm - 1568.2nm
	MCF 4: 1570.6nm - 1587.4nm
Consecutive FBG Bragg-wavelength difference	2.4nm
Gage Factor $(1 - p_e)$	0.737
Interrogator model	FBGS FBG-scan 804D
Fiber coating	ORMOCER®-T
FBG Refractive Index	3%
Number of cores	7 cores – 1 centered, 6 off-centered
Number of FBG sets	8
FBG length	5 mm
Consecutive FBG center to center distance	14 mm
Sensorized fiber length	103 mm

position in 3 dimensions, were used as ground truth in the experiments. As per manufacturer specification, the root mean square error of the sensors is 0.7 mm in position and 0.2 degrees in orientation.

The PBN, with a 15 MPa Young's modulus, is 2.5 mm in diameter and was produced via extrusion (Xograph Healthcare Ltd. - Gloucestershire, United Kingdom) of a medical-grade polymer (plasticized polyvinyl chloride) with 86 Shore "A" hardness. Nano-coating with Poly(para-xylylene) was applied to reduce friction between segments. Each segment of the PBN has 0.25 mm and 0.3 mm outer diameter lumens, which are used to accommodate the MCFs and EM sensors, respectively. Four EM sensors were inserted into the segment lumens in such a way that each sensor was located at one of the segment tips.

The PBN segments were actuated at a predefined speed of 1 mm·s⁻¹, which was stated as suitable for neurosurgery in [6], by an actuation unit consisting of 4 linear actuators. The actuation unit also incorporates encoders, which are used to determine n_k of each segment at each time step. Both the actuation and the shape sensing software were developed in-house in MathWorks MATLAB 2020b. The *ex vivo* experimental setup is shown in Fig. 10 and the PBN during one of the gelatin experiments is captured in Fig 11.
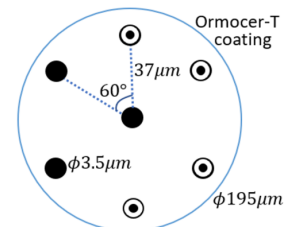

Fig. 9. MCF cross-section including 1 centered and 6 off-centered cores. The 4 cores used in this study are marked with black and white circles.

Four adjacent cores of the MCFs were used in this study (Fig. 9) for shape reconstruction because of the better signal quality with the cores at one half of the cross-section, as a result of the production method.

To enable repeated use of the FBG sets, the fibers need to be able to be removed easily. However, they also need to be fixed to the segments during the insertion process. Therefore, a part was designed, and 3-D printed to fix the fibers to the corresponding segment bases, Fig. 12.

The *in vitro* experiments were conducted in a gelatin soft tissue simulant, and the *ex vivo* experiments were conducted in *ex vivo* brain tissue to test the validity of the proposed methods. In both types of the experiments, the PBN was inserted into the soft mediums using the actuation unit so that it created the following shapes:

1) Single bend: this is a planar curved-shape with a 150 mm radius.
2) Double bend: this is a planar shape with 2 bends along its length. The radius of each bend is 150 mm.
3) 3-D shape: this is similar to the one used in the simulation. It consists of two 60 mm parts and has zero torsion along its length. The first part's radius of curvature is 150 mm. The radius of curvature of the second part, which is in a plane perpendicular to the first one, is 200 mm.

The insertions were completed in such a way that there were always two aligned segments ahead of the other two so that the ground truth PBN tip position and orientation could be computed using the EM sensors attached to the leading segments.

Six insertion experiments (3 *in vitro* and 3 *ex vivo*) were conducted in total, and the PBN was reconstructed online. All the insertions were carried out to a depth of 120 mm, which is longer than the fiber's sensorized length. The tip position and orientation reconstructions for each PBN segment were compared with the ground truth data obtained from the EM sensor attached to the corresponding segment. Thus, validation was performed using the reconstructions of 24 single segments and 6 PBNs in total.
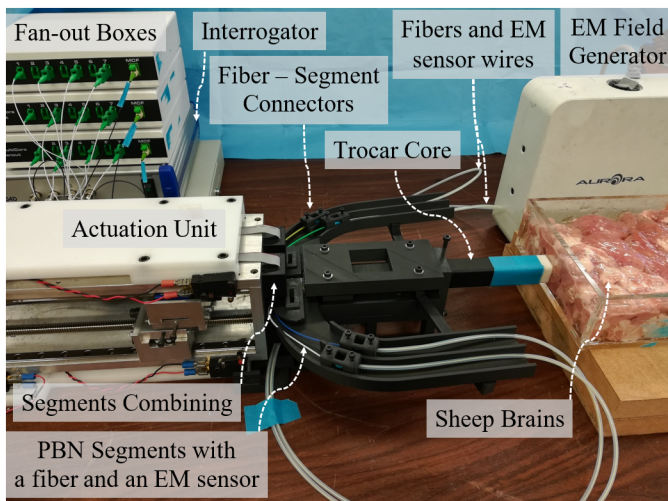
The gelatin phantom was produced from 7% by weight bovine gelatin, which mimics human brain tissue [54]. Sheep brains were purchased from a local butcher, and several of them were used to create a large enough volume for steering to become observable.

R was calculated via the method explained in Section IV-C, and the moving average filter used in the experiments was also taken into account in the determination of R. In order to optimize Q, the PBN instrumented with both optical fibers and EM sensors was inserted into a gelatin phantom in such a way that the PBN created the 3-D shape, which was the one used in experiments, as defined earlier in this section. Then, Q and ρ were optimized with the interior point algorithm using MATLAB 2020b (Mathworks inc.) to minimize the tip position reconstruction error. As a result, the matrices and the scaling factor ρ were determined to be as follows:

$$R = \begin{bmatrix} 0.21 & -0.15 \\ -0.15 & 0.26 \end{bmatrix} m^{-2}, \quad Q = \xi \begin{bmatrix} 2.21 & -0.85 \\ -0.85 & 2.21 \end{bmatrix} m^{-2}$$

$$\rho = 2.04$$

The neutral axis separations were calculated using Dassault Systèmes SolidWorks:

$$d_1 = \begin{bmatrix} 0.40 \\ 0.63 \end{bmatrix} mm, \quad d_2 = \begin{bmatrix} -0.63 \\ 0.40 \end{bmatrix} mm$$

$$d_3 = \begin{bmatrix} -0.40 \\ -0.63 \end{bmatrix} mm, \quad d_4 = \begin{bmatrix} 0.63 \\ -0.40 \end{bmatrix} mm$$

The tip position reconstruction was also performed with an interpolation-based method to compare the proposed method's performance with a standard approach. The reconstruction was made on the basis of the parallel transport frames to use the same method as in the proposed approach after strain interpolation, which is preferred because of the advantages explained in Section III-A. However, the shape could be reconstructed with the interpolation-based method only until an insertion length of 113 mm, as this value corresponds to the

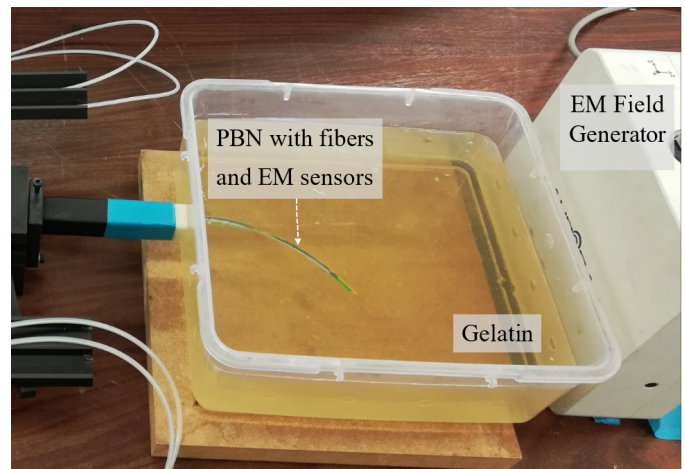Fig. 10. The *ex vivo* experimental setup

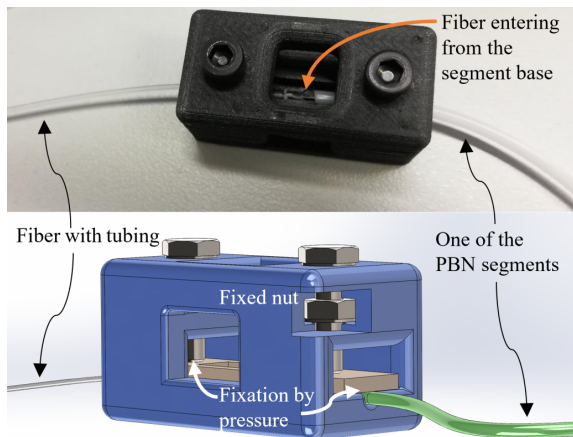Fig. 11. The *in vitro* experimental setup. - The PBN navigating inside the gelatin phantom

Fig. 12. The 3-D printed part fixing the fibers with PBN segment bases

sum of the sensorized fiber length and lead-out length, l_{lead}, the last of which measured as 10 mm.

B. Results

The mean, standard deviation, and maximum of the tip errors for both PBN and individual segment reconstructions were calculated online at each time step over the 120 mm insertion and are presented in Table III and Table IV, for position and orientation, respectively. Fig. 13 shows the PBN tip position reconstruction and the ground truth during the *ex vivo* experiment with the 3-D shape. The single segment results cover all four segments of the PBN. The results of the reconstructions made with the interpolation-based method are given in Table V.

VII. DISCUSSION

The simulation results show that both the interpolation method and the positions of angle discontinuities along a fiber significantly influence the tip position error. By eliminating these uncertainties, shape reconstruction with the proposed method has resulted in the tip position error being decreased to a negligible level in a noise-free simulation environment.

The best experimental results were obtained using all the FBG sets of the fibers, which was expected. It is seen that in this case, the highest mean position error is 2.87 mm, which is in the clinically acceptable margin for tumors with 0.5 ml
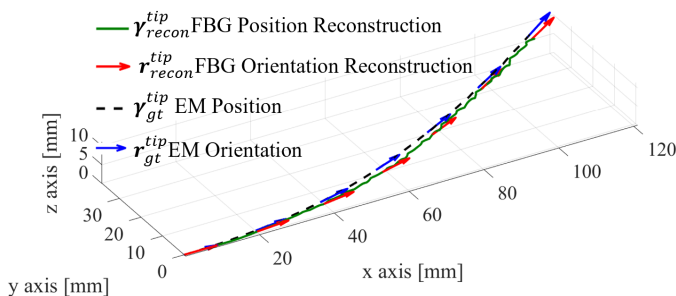

Fig. 13. The EM sensor position measurements and the FBG-based tip pose reconstruction

volume, the limit for clinically significant prostate tumors as reported in [55].

The error values obtained using 8 FBG sets are considerably lower than those obtained with only the tip FBG sets. This is probably because a higher number of FBG sets along a fiber enables better detection of curvature changes due to tissue deformation and leads to more accurate shape reconstruction. Thanks to our KF approach, the FBG sets other than the one at the tip are also used to correct the reconstruction constantly.

Results for the *in vitro* experiments are lower than those for the *ex vivo* experiments, as expected, because of the homogeneity of the soft tissue phantom compared to biological tissue. Navigating through the *ex vivo* tissue might have resulted in slight buckling of the PBN when penetrating tissue layers, and nonuniform deformation of the tissue, which would have affected the needle shape. These cases were accounted for, to a certain extent, by fusing the curvature information of the previously created points with those of new measurements. The results show that our method is capable of dealing with tissue heterogeneity and tissue layers with different mechanical properties. Also, we expect that better results could be obtained with less compliant tissue such as the liver, which would provide better support for the needle to navigate in a follow-the-leader fashion, thanks to its higher stiffness.

The orientation error results are generally in agreement with the position errors. In comparison to the interpolation-based method, similar results were obtained in the case of the Single Bend shape. However, especially when looking at the maximum error values, the performance of the proposed approach seems to outperform the interpolation-based approach in the case of experiments with 3D Shape and Double Bends, for which inflection points were shown to be one of the most significant error sources for the reconstruction methods requiring interpolation.

Compared to our previous work [24], where an FBG-based shape reconstruction method requiring interpolation was used for the dynamic reconstruction of a PBN, the mean tip position and orientation errors decreased significantly. When compared to the results in [27], where the needle shape was reconstructed statically, a higher mean error was obtained in our study. The lower accuracy may be due to the lower signal-to-noise-ratio in the dynamic reconstruction, tissue movements during the dynamic experiments, and the low refractivity of the MCFs produced with the DTG method. This method's advantage, providing durable fibers suitable for dynamic environments, comes at the cost of low refractivity compared to other production methods, such as the Phase Mask technique. Therefore, this leads to lower performance in wavelength detection and, accordingly, higher tip position error.

Another error source with the dynamic experiments can be that the fibers are fixed to the needle only at the needle base, which may not be sufficient to prevent relative motion between needle and fiber under strain. The resulting errors can be mitigated using a needle's mechanics model, such as [9] for PBNs.

Similar to single-core fibers [25], [46], imprecise placement of the MCFs along the needle may be another possible source of error.

TABLE III

MEAN ($\bar{e}_{pos}^{tip}$), STANDARD DEVIATION ($\sigma_{e_{pos}^{tip}}$) AND MAXIMUM ($e_{pos,max}^{tip}$) OF TIP POSITION ERRORS: $\bar{e}_{pos}^{tip}$ ($\sigma_{e_{pos}^{tip}}$) [$e_{pos,max}^{tip}$] (mm)

		PBN (4 MCFs)		Single Segments (1 MCF)	
	Reconstruction with →	Tip FBG set	8 FBG sets	Tip FBG set	8 FBG sets
In vitro	Single Bend	2.03(1.33)[4.72]	1.01(0.51)[2.22]	3.69(1.69)[6.96]	1.77(0.98)[3.57]
	Double Bend	2.24(1.54)[5.10]	1.95(0.98)[4.62]	4.81(1.94)[8.71]	2.09(1.48)[4.99]
	3D Shape	3.08(1.70)[6.25]	2.18(1.30)[4.96]	5.16(2.35)[9.53]	2.95(1.65)[6.12]
Ex vivo	Single Bend	4.69(1.37)[7.12]	1.16(0.64)[2.71]	5.79(1.78)[9.30]	2.10(0.97)[4.05]
	Double Bend	5.60(2.70)[11.84]	2.04(1.01)[5.24]	6.93(2.93)[11.91]	2.27(1.33)[5.32]
	3D Shape	5.42(1.91)[9.95]	2.87(1.63)[5.76]	7.54(3.28)[11.46]	3.24(1.84)[6.87]

TABLE IV

MEAN ($\bar{e}_{o}^{tip}$), STANDARD DEVIATION ($\sigma_{e_{o}^{tip}}$) AND MAXIMUM ($e_{o,max}^{tip}$) OF TIP ORIENTATION ERRORS: $\bar{e}_{o}^{tip}$ ($\sigma_{e_{o}^{tip}}$) [$e_{o,max}^{tip}$] (deg)

		PBN (4 MCFs)		Single Segments (1 MCF)	
	Reconstruction with →	Tip FBG set	8 FBG sets	Tip FBG set	8 FBG sets
In vitro	Single Bend	2.89(1.14)[5.57]	2.47(1.08)[4.19]	3.35(1.50)[6.86]	2.68(1.21)[5.33]
	Double Bend	3.11(1.88)[6.35]	2.51(1.49)[5.67]	3.60(2.12)[7.46]	2.96(1.99)[6.95]
	3D Shape	4.21(2.44)[7.26]	3.43(2.21)[6.41]	4.61(2.59)[8.38]	3.74(2.48)[7.64]
Ex vivo	Single Bend	3.18(2.08)[5.89]	2.33(1.60)[4.66]	4.18(2.59)[7.45]	3.52(2.54)[6.81]
	Double Bend	4.01(2.72)[7.10]	3.78(2.39)[6.71]	5.78(2.83)[10.94]	4.24(2.60)[8.22]
	3D Shape	4.48(2.84)[9.79]	3.84(2.76)[8.29]	6.66(3.01)[12.10]	5.45(2.90)[9.49]

TABLE V

TIP POSITION ERRORS OF SINGLE SEGMENT RECONSTRUCTIONS WITH THE INTERPOLATION-BASED METHOD: $\bar{e}_{pos}^{tip}$ ($\sigma_{e_{pos}^{tip}}$) [$e_{pos,max}^{tip}$] (mm)

	In vitro	*Ex vivo*
Single Bend	2.54(1.16)[4.15]	2.86(1.27)[5.20]
Double Bend	3.66(2.25)[9.91]	4.06(2.76)[11.55]
3D Shape	5.24(2.33)[10.84]	6.1(3.64)[13.29]

Errors can also be attributed to calibration inaccuracies because, as in [45], small errors in wavelength in zero-strain and bending direction with respect to the 1st core, θ, accumulate throughout the MCF length, resulting in significant position error at the tip.

The sampling frequency along the navigation path can be increased to improve the shape reconstruction accuracy by decreasing the insertion speed or increasing the interrogator's sampling frequency. The single evaluation time of the algorithm and the experimental results show that the algorithm can work on an average PC with an adequate sampling frequency to run online.

Although a constant insertion speed was preferred in this study, since the number of curve points created at each time step is computed using the navigation length, our method allows navigation with other speeds or varying speeds for each PBN segment.

In this study, the torsion that the needle is exposed to was assumed to be negligible. However, considering the isotropic material structure of the PBN and the asymmetric forces and deformations that the PBN might have undergone during the navigation in heterogeneous soft tissue, the errors can also be attributed to this assumption. To reduce the resulting errors,

a composite steerable needle could be used with a wire braid that is stiff in torsion and compliant in bending, as suggested in [56]. Alternatively, the torsion can be detected and accounted for using helically-wrapped optical fibers [57], [58].

Lastly, although our results were obtained with a PBN, we believe that they are representative of the performance of other steerable needle designs that operate in a follow-the-leader fashion, given that a single PBN segment can be considered as an independent bevel-tip steerable needle.

VIII. CONCLUSION AND FUTURE WORK

This study presented a novel method for FBG-based shape reconstruction of steerable needles where the needle tip creates the insertion trajectory and is followed by the rest, assuming a follow-the-leader insertion method. Instead of reconstructing the steerable needle's shape, we proposed reconstructing the trajectory created by the needle tip during insertion into soft tissue under the assumption that the needle shape and the trajectory created by the needle tip are equivalent. This leads to the possibility of shape reconstruction even in the presence of 1 FBG set only, located at the needle tip. This approach, independently of the number of FBG sets used, also removes the limit that the reconstruction length can only be so long as the length of the sensorized region which is, to the best of our knowledge, a first in FBG-based steerable needle shape reconstruction. Besides, a KF-based sensor fusion method was introduced to combine the sensory information of a specific location on the trajectory acquired at different times. We also proposed a fusion method for combining the sensory information from different sensors for the case where more than 1 FBG set is present along an MCF. We assessed the performance of the methods in both simulation and experiments with a clinically-sized PBN. The lead-out length, which

is between the needle tip and the last FBG set, was taken into account, and the errors were calculated with respect to the PBN tip and PBN segment tips. *In vitro* and *ex vivo* dynamic experiments in both 2-D and 3-D were conducted to validate the proposed methods and demonstrate clinically acceptable tracking accuracy. Finally, the effect of bending direction discontinuities on shape reconstruction accuracy was investigated with a simulation study.

This method can enable effective closed-loop control of a PBN along a desired three-dimensional trajectory. As future work, based on the proposed shape reconstruction method, investigations of curvature tracking controllers for trajectory following of a steerable needle are planned.

References

[1] N. Abolhassani, R. Patel, and M. Moallem, "Needle insertion into soft tissue: A survey," *Medical Engineering and Physics*, vol. 29, no. 4, pp. 413–431, 2007.

[2] N. J. Van De Berg, D. J. Van Gerwen, J. Dankelman, and J. J. Van Den Dobbelsteen, "Design Choices in Needle Steering - A Review," *IEEE/ASME Transactions on Mechatronics*, vol. 20, no. 5, pp. 2172–2183, 2015.

[3] M. Scali, T. P. Pusch, P. Breedveld, and D. Dodou, "Needle-like instruments for steering through solid organs: A review of the scientific and patent literature," *Proceedings of the Institution of Mechanical Engineers, Part H: Journal of Engineering in Medicine*, vol. 231, no. 3, pp. 250–265, 2017.

[4] U. Cerkvenik, B. Van De Straat, S. W. Gussekloo, and J. L. Van Leeuwen, "Mechanisms of ovipositor insertion and steering of a parasitic wasp," in *Proceedings of the National Academy of Sciences of the United States of America*, vol. 114, no. 37, 2017, pp. E7822–E7831.

[5] M. J. Oldfield, A. Leibinger, T. E. T. Seah, and F. Rodriguez y Baena, "Method to Reduce Target Motion Through Needle–Tissue Interactions," *Annals of Biomedical Engineering*, vol. 43, no. 11, pp. 2794–2803, 2015.

[6] E. Matheson, T. Watts, R. Secoli, and F. Rodriguez y Baena, "Cyclic Motion Control for Programmable Bevel-Tip Needle 3D Steering: A Simulation Study," in *IEEE Int Conference on Robotics and Biomimetics, ROBIO 2018*. Kuala Lumpur, Malaysia: IEEE, 2018, pp. 444–449.

[7] M. C. Bernardes, B. V. Adorno, P. Poignet, and G. A. Borges, "Robot-assisted automatic insertion of steerable needles with closed-loop imaging feedback and intraoperative trajectory replanning," *Mechatronics*, vol. 23, no. 6, pp. 630–645, 2013. [Online]. Available: http://dx.doi.org/10.1016/j.mechatronics.2013.06.004

[8] R. Secoli and F. Rodriguez y Baena, "Experimental Validation of Curvature Tracking with a Programmable Bevel-Tip Steerable Needle," in *Inter. Symposium on Medical Robotics (ISMR)*, 2018.

[9] T. Watts, R. Secoli, and F. Rodriguez y Baena, "A Mechanics-Based Model for 3-D Steering of Programmable Bevel-Tip Needles," *IEEE Transactions on Robotics*, vol. 35, no. 2, pp. 371–386, 2018.

[10] T. K. Poddler, D. P. Clark, J. Sherman, D. Fuller, E. M. Messing, D. J. Rubens, J. G. Strang, Y. D. Zhang, W. O'Dell, W. S. Ng, and Y. Yu, "Effects of Tip Geometry of Surgical Needles: An Assessment of Force and Deflection," in *The 3rd European Medical and Biological Engineering Conference*, Prague, Czech Republic, 2005.

[11] C. Shi, X. Luo, P. Qi, T. Li, S. Song, Z. Najdovski, T. Fukuda, and H. Ren, "Shape Sensing Techniques for Continuum Robots in Minimally Invasive Surgery: A Survey," *IEEE Transactions on Biomedical Engineering*, vol. 64, no. 8, pp. 1665–1678, 2017.

[12] F. Monet, S. Sefati, P. Lorre, A. Poiffaut, S. Kadoury, M. Armand, I. Iordachita, and R. Kashyap, "High-Resolution Optical Fiber Shape Sensing of Continuum Robots: A Comparative Study ," in *Proceedings - IEEE International Conference on Robotics and Automation*, 2020, pp. 8877–8883.

[13] A. M. Franz, T. Haidegger, W. Birkfellner, K. Cleary, T. M. Peters, and L. Maier-Hein, "Electromagnetic tracking in medicine - A review of technology, validation, and applications," *IEEE Transactions on Medical Imaging*, vol. 33, no. 8, pp. 1702–1725, 2014.

[14] N. Shahriari, R. J. Roesthuis, N. J. Van De Berg, J. J. Van Den Dobbelsteen, and S. Misra, "Steering an actuated-tip needle in biological tissue: Fusing FBG-sensor data and ultrasound images," in *Proceedings - IEEE International Conference on Robotics and Automation*, vol. 2016. Stockholm, Sweden: IEEE, 2016.

[15] M. Abayazid, P. Moreira, N. Shahriari, S. Patil, R. Alterovitz, and S. Misra, "Ultrasound-guided three-dimensional needle steering in biological tissue with curved surfaces," *Medical Engineering and Physics*, vol. 37, no. 1, pp. 145–150, 2015. [Online]. Available: http://dx.doi.org/10.1016/j.medengphy.2014.10.005

[16] D. Glozman and M. Shoham, "Image-Guided Robotic Flexible Needle Steering," *IEEE Transactions on Robotics*, vol. 23, no. 3, pp. 459–467, 2007.

[17] N. Shahriari, E. Hekman, M. Oudkerk, and S. Misra, "Design and evaluation of a computed tomography (CT)-compatible needle insertion device using an electromagnetic tracking system and CT images," *International Journal of Computer Assisted Radiology and Surgery*, vol. 10, pp. 1845–1852, 2015. [Online]. Available: http://dx.doi.org/10.1007/s11548-015-1176-3

[18] S. P. DiMaio, E. Samset, G. Fischer, I. Iordachita, G. Fichtinger, F. Jolesz, and C. Tempany, "Dynamic MRI Scan Plane Control for Passive Tracking of Instruments and Devices," in *Medical Image Computing and Computer-Assisted Intervention - MICCAI*, 2007.

[19] F. Taffoni, D. Formica, P. Saccomandi, G. Di Pino, and E. Schena, "Optical fiber-based MR-compatible sensors for medical applications: An overview," *Sensors*, vol. 13, no. 10, pp. 14 105–14 120, 2013.

[20] Y. L. Park, S. Elayaperumal, B. Daniel, S. C. Ryu, M. Shin, J. Savall, R. J. Black, B. Moslehi, and M. R. Cutkosky, "Real-time estimation of 3-D needle shape and deflection for MRI-guided interventions," *IEEE/ASME Transactions on Mechatronics*, vol. 15, no. 6, pp. 906–915, 2010.

[21] K. Henken, D. Van Gerwen, J. Dankelman, and J. Van Den Dobbelsteen, "Accuracy of needle position measurements using fiber Bragg gratings," *Minimally Invasive Therapy and Allied Tech.*, vol. 21, no. 6, pp. 408–414, 2012.

[22] R. J. Roesthuis, M. Kemp, J. J. Van Den Dobbelsteen, and S. Misra, "Three-dimensional needle shape reconstruction using an array of fiber Bragg grating sensors," *IEEE/ASME Transactions on Mechatronics*, vol. 19, no. 4, pp. 1115–1126, 2014.

[23] Y. Chitalia, N. J. Deaton, S. Jeong, N. Rahman, and J. P. Desai, "Towards FBG-Based Shape Sensing for Micro-Scale and Meso-Scale Continuum Robots with Large Deflection," *IEEE Robotics and Automation Letters*, vol. 5, no. 2, pp. 1712–1719, 2020.

[24] F. Khan, A. Donder, S. Galvan, F. Rodriguez y Baena, and S. Misra, "Pose Measurement of Flexible Medical Instruments using Fiber Bragg Gratings in Multi-Core Fiber," *IEEE Sensors J.*, vol. 20, no. 18, 2020.

[25] H. Pauer, C. Ledermann, W. Tuschmann, and H. Woern, "Non-linear compensation of production inaccuracies and material drift by adjusting the sensor data fusion algorithms for shape sensing based on FBG-optical fibers," in *Processing of 2014 International Conference on Multisensor Fusion and Information Integration for Intelligent Systems, MFI 2014*. IEEE, 2014, pp. 1–5.

[26] J. P. Moore and M. D. Rogge, "Shape sensing using multi-core fiber optic cable and parametric curve solutions," *Optics Express*, vol. 20, no. 3, p. 2967, 2012.

[27] F. Khan, A. Denasi, D. Barrera, J. Madrigal, S. Sales, and S. Misra, "Multi-core Optical Fibers with Bragg Gratings as Shape Sensor for Flexible Medical Instruments," *IEEE Sensors Journal*, 2019. [Online]. Available: https://ieeexplore.ieee.org/document/8667346/

[28] J. Cui, S. Zhao, C. Yang, and J. Tan, "Parallel transport frame for fiber shape sensing," *IEEE Photonics Journal*, vol. 10, no. 1, pp. 1–12, 2018.

[29] D. Paloschi, K. A. Bronnikov, S. Korganbayev, A. A. Wolf, A. Dostovalov, and P. Saccomandi, "3D Shape Sensing with Multicore Optical Fibers: Transformation Matrices Versus Frenet-Serret Equations for Real-Time Application," *IEEE Sensors Journal*, vol. 21, no. 4, pp. 4599–4609, 2021.

[30] R. Seifabadi, E. E. Gomez, F. Aalamifar, G. Fichtinger, and I. Iordachita, "Real-time tracking of a bevel-tip needle with varying insertion depth: Toward teleoperated MRI-guided needle steering," in *IEEE International Conference on Intelligent Robots and Systems*, Tokyo, Japan, 2013, pp. 469–476.

[31] M. Li, G. Li, B. Gonenc, X. Duan, and I. Iordachita, "Towards human-controlled, real-time shape sensing based flexible needle steering for MRI-guided percutaneous therapies," *The international journal of medical robotics and computer assisted surgery*, vol. 13, 2017.

[32] S. Sefati, R. Hegeman, F. Alambeigi, I. Iordachita, and M. Armand, "FBG-Based Position Estimation of Highly Deformable Continuum

Manipulators: Model-Dependent vs. Data-Driven Approaches," in *2019 International Symposium on Medical Robotics, ISMR 2019*. IEEE, 2019, pp. 1–6.

[33] P. Sears and P. Dupont, "A steerable needle technology using curved concentric tubes," in *IEEE International Conference on Intelligent Robots and Systems*, Beijing, China, 2006, pp. 2850–2856.

[34] A. Denasi, F. Khan, K. J. Boskma, M. Kaya, C. Hennersperger, R. Gobl, M. Tirindelli, N. Navab, and S. Misra, "An Observer-Based Fusion Method Using Multicore Optical Shape Sensors and Ultrasound Images for Magnetically-Actuated Catheters," in *IEEE International Conference on Robotics and Automation*, Brisbane, Australia, 2018, pp. 50–57.

[35] A. Assa and F. Janabi-Sharifi, "A Kalman filter-based framework for enhanced sensor fusion," *IEEE Sensors Journal*, vol. 15, no. 6, pp. 3281–3292, 2015.

[36] W. Elmenreich, "An introduction to sensor fusion," *Austria: Vienna University Of Technology*, no. February, pp. 1–28, 2002.

[37] B. Jiang, W. Gao, D. Kacher, E. Nevo, B. Fetics, T. C. Lee, and J. Jayender, "Kalman filter-based EM-optical sensor fusion for needle deflection estimation," *International Journal of Computer Assisted Radiology and Surgery*, vol. 13, no. 4, pp. 573–583, 2018. [Online]. Available: https://doi.org/10.1007/s11548-018-1708-8

[38] H. Sadjadi, K. Hashtrudi-Zaad, and G. Fichtinger, "Fusion of electromagnetic trackers to improve needle deflection estimation: Simulation study," *IEEE Transactions on Biomedical Engineering*, vol. 60, no. 10, pp. 2706–2715, 2013.

[39] A. Favaro, R. Secoli, F. R. Y. Baena, and E. D. Momi, "Model-Based Robust Pose Estimation for a Multi-Segment, Programmable Bevel-Tip Steerable Needle," *IEEE Robotics and Automation Letters*, vol. 5, no. 4, pp. 6780–6787, 2020.

[40] E. M. Lally, M. Reaves, E. Horrell, S. Klute, and M. E. Froggatt, "Fiber optic shape sensing for monitoring of flexible structures," *Sensors and Smart Structures Technologies for Civil, Mechanical, and Aerospace Systems 2012*, vol. 8345, no. May, p. 83452Y, 2012.

[41] M. Amanzadeh, S. M. Aminossadati, M. S. Kizil, and A. D. Rakić, "Recent developments in fibre optic shape sensing," *Measurement: Journal of the International Measurement Confederation*, vol. 128, no. June, pp. 119–137, 2018.

[42] K. O. Hill and G. Meltz, "Fiber Bragg grating technology fundamentals and overview," *Journal of Lightwave Technology*, vol. 15, no. 8, pp. 1263–1276, 1997.

[43] J. Langer and D. A. Singer, "Lagrangian aspects of the Kirchhoff elastic rod," *SIAM Review*, vol. 38, no. 4, pp. 605–618, 1996.

[44] R. C. Hibbeler, *Mechanics of Materials*, 8th ed. Upper Saddle River, NJ, USA: Pearson Prentice Hall, 2011.

[45] S. Jäckle, T. Eixmann, H. Schulz-Hildebrandt, G. Hüttmann, and T. Pätz, "Fiber optical shape sensing of flexible instruments for endovascular navigation," *International Journal of Computer Assisted Radiology and Surgery*, vol. 14, no. 12, pp. 2137–2145, 2019. [Online]. Available: https://doi.org/10.1007/s11548-019-02059-0

[46] K. R. Henken, J. Dankelman, J. J. V. D. Dobbelsteen, L. K. Cheng, and M. S. V. D. Heiden, "Error Analysis of FBG-Based Shape Sensors for Medical Needle Tracking," *IEEE/ASME Transactions on Mechatronics*, vol. 19, no. 5, pp. 1523–1531, 2014.

[47] B. Raton, *Modern Differential Geometry of Curves and Surfaces with Mathematica*. Florida, USA: Chapman & Hall/CRC, 2006.

[48] A. J. Hanson and H. Ma, "Quaternion Frame Approach to Streamline Visualization," *IEEE Transactions on Visualization and Computer Graphics*, vol. 1, no. 2, pp. 164–174, 1995.

[49] R. L. Bishop, "There is More than One Way to Frame a Curve," *The American Mathematical Monthly*, 1975.

[50] D. Simon, *Optimal state estimation: Kalman, H, and nonlinear approaches*, 2006.

[51] R. H. Byrd, M. E. Hribar, and J. Nocedal, "An interior point algorithm for large-scale nonlinear programming," *SIAM Journal on Optimization*, vol. 9, no. 4, pp. 877–900, 1999.

[52] S. S. Chugh, R. C. Chan, S. B. Johnson, and D. L. Packer, "Catheter tip orientation affects radiofrequency ablation lesion size in the canine left ventricle," *PACE - Pacing and Clinical Electrophysiology*, vol. 22, no. 3, pp. 413–420, 1999.

[53] "FBGS - DTG® Technique." [Online]. Available: https://fbgs.com/technology/dtg-fsg-technology/ Date Accessed: 26 April 2020

[54] G. Franceschini, "The Mechanics of Human Brain Tissue," *Modelling, Preservation and Control of Materials and Structures. University of Trento, Trento, Italy*, 2006.

[55] J. B. Bak, S. K. Landas, and G. P. Haas, "Characterization of Prostate Cancer Missed by Sextant Biopsy," *Clinical Prostate Cancer*, vol. 2, no. 2, pp. 115–118, 2003. [Online]. Available: http://dx.doi.org/10.3816/CGC.2003.n.019

[56] S. C. Ryu and P. E. Dupont, "FBG-based shape sensing tubes for continuum robots," in *Proceedings - IEEE International Conference on Robotics and Automation*, Hong Kong, China, 2014, pp. 3531–3537.

[57] K. C. Galloway, Y. Chen, E. Templeton, B. Rife, I. S. Godage, and E. J. Barth, "Fiber Optic Shape Sensing for Soft Robotics," *Soft Robotics*, vol. 6, no. 5, pp. 671–684, 2019.

[58] R. Xu, A. Yurkewich, and R. V. Patel, "Curvature, Torsion, and Force Sensing in Continuum Robots Using Helically Wrapped FBG Sensors," *IEEE Robotics and Automation Letters*, vol. 1, no. 2, pp. 1052–1059, 2016.

Abdulhamit Donder received the B.Eng. degree in mechanical engineering with the highest ranking in the Faculty of Engineering from Uludağ University, Bursa, Turkey, in 2014, for which he spent a term enrolled at Politecnico di Torino, Turin, Italy. He then received the M.Sc. degree in mechanical engineering from Middle East Technical University, Ankara, Turkey, in 2017.

He is currently pursuing the Ph.D. degree at the Mechatronics in Medicine Laboratory, Imperial College London, London, U.K.

His current research interests include design, sensing, and control of surgical robots.

Ferdinando Rodriguez y Baena (Member, IEEE) received the M.Eng. degree in Mechatronics and Manufacturing Systems Engineering from King's College London, U.K., in 2000, and the Ph.D. degree in Medical Robotics from Imperial College London, in 2004.

He is Professor of Medical Robotics in the Department of Mechanical Engineering at Imperial College, where he leads the Mechatronics in Medicine Laboratory and the Applied Mechanics Division. He is also the Engineering Co-Director of the Hamlyn Centre, which is part of the Institute of Global Health Innovation, since July 2020.

His research interests include mechatronic systems for diagnostics, surgical training, and surgical intervention.